Hot Surface Ionic Line Emission and Cold K-Inner-Shell Emission From Petawatt-Laser-Irradiated Cu Foil Targets

Introduction

There is much interest in both experimental and theoretical studies of laser–solid target interactions with picosecond laser beams at relativistic intensities because of their relevance to fast ignition in laser fusion[1] and backlighter development.[2,3] High-intensity, ultrashort laser pulses impinging onto solid or gaseous targets produce large quantities of suprathermal electrons ranging from ~100 keV up to several MeV with conversion efficiencies of several tens of a percent from the incident laser energy into electron energy.[4–7] A precise physical understanding of the MeV electron production and transport in dense plasma is crucial for the success of the fast-ignition concept. This has triggered vigorous research efforts in both experimental[8–12] and theoretical studies.[13–16]

Strong self-generated magnetic and electric fields influence the transport of relativistic electrons in high-energy-density plasmas.[12,15,17] Inhibited heat flux in insulators due to strong longitudinal electrical fields has recently been predicted at subrelativistic intensities with a one-dimensional Monte Carlo collisional particle-in-cell (PIC) code.[18] Depending on the experimental conditions, the fields might collimate the electron beam or compromise the effectiveness of electron penetration because of flux inhibition.[17,19,20] The guiding of electrons with MeV energy in a plasma fiber over a distance of ~1 mm is attributed to strong laser-generated fields.[21] Many plasma processes influence the heating of solid matter by laser-generated relativistic electrons and their return currents. One example is an observed annular heating pattern that is attributed to a strong Weibel instability growth because of sharp transverse gradients in the input electron-beam current.[11]

Hard x-ray bremsstrahlung and characteristic inner-shell line emissions, predominantly from the K shell, are produced when energetic electrons propagate into the bulk of a solid target. The measurement of inner-shell emission lines is a valuable diagnostic to characterize the suprathermal electron distribution.[4,6,7,22–24] Measurements of electron temperatures and temperature gradients provide important guidance for simulations to study energy transport in relativistic laser–solid density plasmas. The standard method used to infer electron density and temperature in laser-produced plasmas is x-ray line spectroscopy;[25] this method has been applied to petawatt laser–plasma experiments, e.g., Koch *et al*., using aluminum K-shell spectra.[11] The dense and hot plasma environment shifts and broadens the spectral lines because of the interactions of the charged-particle plasma constituents. The comparison of measured line shapes and line ratios with calculations then allows the plasma parameters to be inferred.

In this work, measurements of the surface electron temperatures for petawatt-laser-produced copper plasmas are presented. Measurements of the scaling of the Cu K-shell emission with laser intensity and target thickness are shown and analyzed. The following three sections will present the **Experimental Setup** (p. 208), **Experimental Results** (p. 209), and **Analysis and Discussion** (p. 213). The third section contains two subsections: Resonance-Line Emission From Hot Plasmas (p. 213) and Inner-Shell Emission (p. 216), which compares the measured K_α laser-intensity scaling to a model calculation. **Summary and Conclusions** (p. 218) are presented in the last section.

Experimental Setup

A schematic of the experimental setup is shown in Fig. 104.47. Laser pulses from either the Rutherford Appleton Laboratory Petawatt (PW)[26] or the 100-TW[27] facilities were focused with *f*/3 off-axis parabolas to a spot size of the order of ~10 μm in diameter.[28] The fraction of the nominal laser energy transported onto the target through the compressor and subsequent optics of the PW and the 100-TW laser systems is 75% and 60% respectively. About half of this energy is contained in the main focal spot while the remainder is distributed over a larger area.[28,29] The laser energy was measured for each shot before the beam entered the compressor. The maximum achievable intensities on target were $4(\pm 2) \times 10^{20}$ W/cm^2 and $4(\pm 2) \times 10^{19}$ W/cm^2 with the PW and the 100-TW lasers, respectively. The relatively large uncertainty in intensity on target is mainly due to changes in the focal-spot pattern on a shot-to-shot basis.

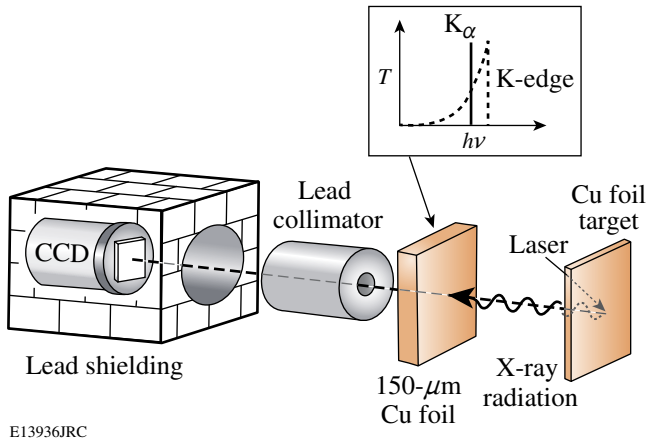

Figure 104.47
Experimental setup. The petawatt laser is focused onto a thin copper foil target. A single-hit CCD camera measures the x-ray emission from the target's front side. Lead collimators and lead shielding provide the necessary suppression of unwanted background radiation. A 150-μm copper foil provides bandpass filtering of the Cu K-shell emission while suppressing the background radiation. The inset shows qualitatively the foil transmission versus photon energy and the position of the K_α line.

Preplasma formation was measured side-on with a frequency-doubled, 1-ps probe beam and a Wollaston prism interferometer, which showed that the plasma surface with an electron density of 10^{19} cm^{-3} expands at most by 40 μm from the original target surface at 100 ps prior to the main pulse interaction. Higher electron densities are not accessible by this diagnostic because of probe-light refraction out of the *f* number of the collecting lens in the probe line. Prepulse measurements show an amplified spontaneous emission (ASE) pulse starting at 1.5 ns ahead of the main pulse with an intensity of 5×10^{-8} of the main pulse intensity. The overall intensity contrast is better than 10^5 in a time window between 10 ns and 50 ps before the main pulse.[28] The *p*-polarized light was focused at a 30° angle of incidence onto thin (<30 μm) copper foil targets with an area of <2000 × 2000 μm^2. The targets were mounted as flags on 6-μm-diam carbon fibers.

A single-photon–counting, x-ray back-illuminated, charge-coupled-device (CCD) camera (SI 800-145, Spectral Instruments-Photonics, Tucson AZ) measured the plasma emission from the laser irradiation side ("target front side") at a viewing angle of 16° with respect to the target normal. Radiation shielding of the CCD camera with a lead housing and lead collimators was crucial in obtaining good signal-to-noise spectra by suppressing the hard x-ray background generated by the petawatt laser.[30] In addition, a 150-μm-thick Cu foil filter in front of the CCD was used to adjust the signal level of the K-shell emission to the single-photon–counting regime and to improve the signal-to-noise ratio. The experimental setup with the 100-TW facility was similar to that described above. The CCD detector was located closer to the plasma source in that case, 1.4 m instead of 3.8 m, leading to an increased solid angle by a factor of ~7.

When an x-ray photon is absorbed in the material of the CCD, a certain number of free-charge carriers proportional to the x-ray photon energy are created. A significant number of x-ray events are split between adjacent pixels. Adding the value of the pixels surrounding the event centroid might be used to reconstruct the total charge collected from an event. This is useful at very low photon fluxes, especially in astronomical applications. The single pixel analysis, as used here, ignores the spread of the absorbed x-ray energy over several pixels and typically takes only ~20% of the absorbed 8 to 9 keV photons into account.[31] Single pixel analysis has a slightly higher spectral resolution than summed pixel analysis.[31,32] A CCD quantum efficiency of ~10% with single pixel analysis is reported in the 8 to 9 keV range for an x-ray imaging spectrometer used in the x-ray astronomical satellite Astro-E.[31] A quantum-efficiency measurement of a SI-800 camera at 8 keV revealed a value of ~5% with single-pixel analysis.[33] The same kind of chip (CCD42-40 chip, e2v technologies, Chelmsford UK) was used in the two SI cameras, one for calibration and one in this experiment. The quantum efficiency is a factor 2 lower compared to the Astro-E CCD, which is probably due to a smaller pixel size and a thinner depletion layer of the SI-800 chip.

Experimental Results

Figure 104.48 shows a copper K-shell spectrum from the target's front side for laser shot 0311271. Laser pulses with an energy of 447 J and a pulse duration ~0.7 ps were focused to an intensity of ~3 × 10^{20} W/cm^2 onto a 20-μm-thick Cu foil target. The continuum x-ray background is subtracted while the filter transmission of the 150-μm Cu foil has not yet been taken into account. The measured spectrum (dashed curve) consists of four overlapping lines. The other curves denote a fit of Gaussian line shapes to the measurement, indicating a full width at half maximum of ~220 eV for each line. The four peaks are identified as the lines of the Cu K_α (8.04 keV), He_α (8.35 keV), Ly_α (8.69 keV), and K_β (8.91 keV) transitions.[34,35] The He_α line dominates the spectrum. The observation of He_α and Ly_α is distinctly different from Cu K-shell spectra observed previously with ultrashort laser pulses at lower laser intensities.[24] The appearance and intensity of the He_α and Ly_α lines depend strongly on the laser intensity, as shown in Fig. 104.49. The K-shell emission was measured with 0.7 ps pulses for

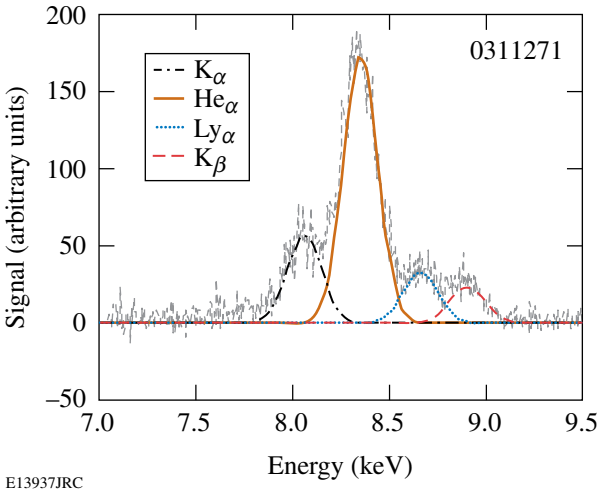

Figure 104.48
Copper K-shell spectrum from the target's front side for a laser intensity of 3×10^{20} W/cm^2 and a pulse duration of 0.7 ps and E_L = 447 J. The gray curve denotes the measurement while the other curves are Gaussian fits to the various emission lines. The He$_\alpha$ resonance line of helium-like copper ion dominates the spectrum.

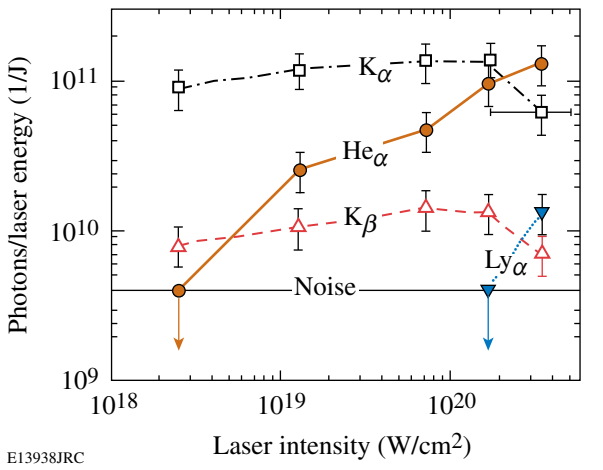

Figure 104.49
Integral x-ray photon number normalized to the laser energy contained in the central laser spot as a function of the laser intensity for Cu K$_\alpha$ (open squares), He$_\alpha$ (solid dots), K$_\beta$ (open triangles), and Ly$_\alpha$ (solid inverted triangles). Square Cu foils with thicknesses of 20 μm and 30 μm and areas ranging from 500×500 μm^2 through 2000×2000 μm^2 were used. The intensity was varied by the focal spot (10 to 100 μm) and the beam energy (~200 to ~500 J) while keeping the pulse duration constant at 0.7 ps. The apparent threshold of Ly$_\alpha$ is 3×10^{20} W/cm^2, while only K$_\alpha$ and K$_\beta$ are observed at 2.5×10^{18} W/cm^2. A representative error bar of the laser intensity is shown for one K$_\alpha$ data point.

various laser intensities between ~2×10^{18} W/cm^2 and ~3×10^{20} W/cm^2 by varying the spot size within 10 to 100 μm and the beam energy in the range from ~200 J to ~500 J. The Ly$_\alpha$ line of hydrogen-like copper disappears below 3×10^{20} W/cm^2, while He$_\alpha$ is observed down to 1×10^{19} W/cm^2, and only K$_\alpha$ and K$_\beta$ are measured at 2.5×10^{18} W/cm^2. No measurements with 0.7-ps pulses are available between 2.5×10^{18} W/cm^2 and 1×10^{19} W/cm^2. Additional measurements in this intensity range with longer pulses (5 to 14 ps) show the He$_\alpha$ signal down to ~6×10^{17} W/cm^2. For 0.7-ps pulses, the noise level prevents the detection of He$_\alpha$ below 3×10^{18} W/cm^2, while for higher intensities it is always measured and steadily increases with laser intensity. In contrast, K$_\alpha$ and K$_\beta$ stay about constant between 2×10^{18} W/cm^2 and 1×10^{20} W/cm^2 and slightly decrease for intensities above 10^{20} W/cm^2.

The absolute number of x-ray photons in each line normalized to the laser energy contained in the central laser spot was calculated by integrating the number of hits and by taking the solid angle, filter transmission, and quantum efficiency of the CCD in single-pixel analysis mode into account. An isotropic emission into a 4π steradians solid angle is assumed. Reabsorption of the radiation inside the foil target has not been taken into account. The relative error bars are estimated to be ~30% based on the standard deviation of several measurements at the same intensity. The absolute error is estimated to be a factor of 2 based on an estimated uncertainty in the CCD quantum efficiency for single-pixel analysis.

The Cu K-shell spectrum was studied as a function of the foil thickness with the 100-TW laser facility for low-mass, small-area targets. Figure 104.50 shows the measured K$_\alpha$, He$_\alpha$, and K$_\beta$ lines for Cu foils of various thicknesses. Laser pulses with 14 ps (a) and 10 ps [(b)–(d)] durations and beam energies of ~100 J were focused to an ~10-μm spot size, providing an intensity of ~3×10^{18} W/cm^2. The thickness is indicated in each figure. The foil area was 500×500 μm^2 in (a) while it was 100×100 μm^2 in (b), (c), and (d). The ratio of K$_\alpha$ to He$_\alpha$ emission changes with thickness, and the relative helium-like emission becomes larger with thinner foils for the smaller areas. Only a limited number of spectra were sampled, however, and shot-to-shot fluctuations especially influence the He$_\alpha$ signal. The resulting x-ray photon number per laser energy is plotted semilogarithmically as a function of the foil thickness in Fig. 104.51. The cold inner-shell emission that is created mainly by suprathermal electrons traversing the foil behaves differently than the ionic line emission. The K$_\alpha$ signal is relatively independent of foil thickness. A significant decrease is observed only below 3 μm, which might be due to

several effects: (1) an increased volumetric heating might lead to a depletion of cold material and (2) an increased transfer of hot-electron energy into channels other than K_α emission for very low volume targets, notably ion acceleration,[36,37] might quench the inner-shell signal. The K_β intensity drops by a factor of ~4 from 30 μm to 20 μm, and then stays about constant with smaller thicknesses and decreases again below 3 μm. The strong decrease from 30 μm to 20 μm is probably due to the larger foil area, which is further discussed in **Resonance-Line Emission From Hot Plasmas** (p. 213). While the inner-shell x-ray photon number decreases with thinner foils, the ionic line emission seems to show an opposite trend for large thicknesses. The He_α signal first increases with diminishing thickness, peaks at 5 μm, and then decreases to its initial value at 1 μm. The relatively large scattering of the values is probably due to shot-to-shot fluctuations in the laser conditions and the focus position on the small target.

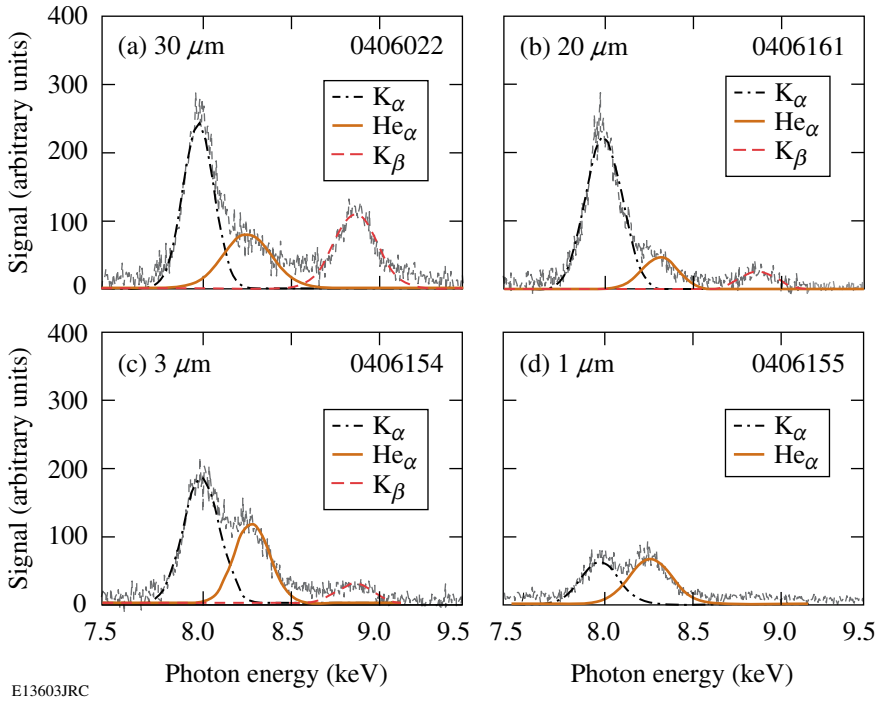

Figure 104.50
K-shell spectra showing the K_α, He_α, and K_β lines for various Cu foil thicknesses as is indicated in each figure. The foil areas were 500×500 μm^2 (a) and 100×100 μm^2 for the measurements in (b)–(d). The laser energies in (a)–(d) were 102 J, 118 J, 116 J, and 97 J, respectively. Laser pulses with 14-ps (a) and 10-ps (b)–(d) durations were focused to an ~10 μm spot, providing intensities of $\sim 3 \times 10^{18}$ W/cm^2.

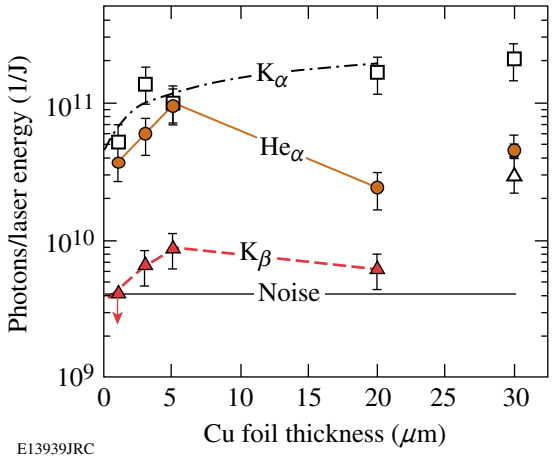

Figure 104.51
X-ray photon number per laser energy in the central laser spot versus foil thickness determined from the measured cold K_α, K_β, and the hot He_α emission. The experimental conditions are the same as in Fig. 104.50. The dash–dotted curve is a guide for the eye. The foil volume diminished from 30 μm to 20 μm by a factor of ~40 because of the smaller area. An increased volume heating probably depletes the copper M-shell population, yielding a decreased K_β signal while the K_α is not significantly affected.[55]

Evidence that the ionic emission originates from front-surface plasmas was obtained from measurements of Cu-foil targets covered with a thin layer of a different material. Figures 104.52(a)–104.52(c) show spectra at an intensity of 1.5×10^{20} W/cm^2 on copper-foil targets without a cover layer (a), with a 1-μm-thick aluminum layer (b), and with a 0.5-μm-thick tantalum layer (c). The comparison of (a) and (b) shows that the He$_\alpha$ emission is significantly reduced by a factor of ~5, while K$_\alpha$ and K$_\beta$ are diminished by a factor of ~2. The data suggest that, with the Al coating, the hot plasma is created mainly in the aluminum with relatively little heating of the copper. The reduction in K$_\alpha$ and K$_\beta$ may indicate stopping of hot electrons in the Al layer. The Ly$_\alpha$ is not observed at this laser intensity. An additional experiment, Fig. 104.52(c), at the same intensity with a 0.5-μm Ta overcoat on 20-μm Cu foil gives further evidence that the Cu He$_\alpha$ line emission originates from a thin layer on the target's front side. Beside the Cu K$_\alpha$ and a strong L-shell emission from tantalum peaking at 8.75 keV, no Cu He$_\alpha$ line at 8.35 keV is measured. The mass densities of solid tantalum and aluminum are 16.7 g/cm^3 and 2.7 g/cm^3, respectively. The factor of 6 higher mass density explains why Ta is more efficient in blocking energy transport through the surface despite half of the film thickness, leading to plasma temperature at the Ta–Cu boundary that is not sufficient to generate He-like Cu ions.

It is interesting to compare the result from copper (Z = 29) to the K-shell emission of a target material with a much higher atomic number. Figure 104.53 shows the result of an experiment with a 50-μm-thick silver foil target (Z = 47) at ~2×10^{20} W/cm^2. Only the inner-shell emission (but no He$_\alpha$ and Ly$_\alpha$ lines) is observed for the higher-Z target. This indicates that the temperature is not high enough to create He- and H-like silver ions, which require estimated electron temperatures above ~50 keV.[38]

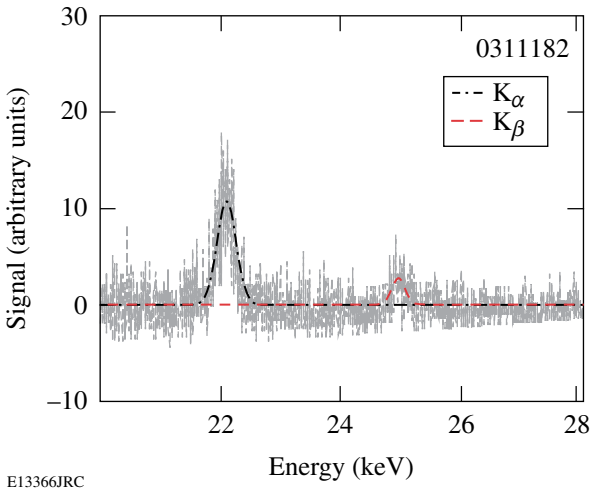

Figure 104.53
Measurement of the silver K-shell emission from a 50-μm-thick Ag-foil target. The laser energy, pulse duration, and intensity were 275 J, 0.7 ps, and ~2×10^{20} W/cm^2, respectively. Only K$_\alpha$ and K$_\beta$ inner-shell emission lines are measured, but not the ionic line emission.

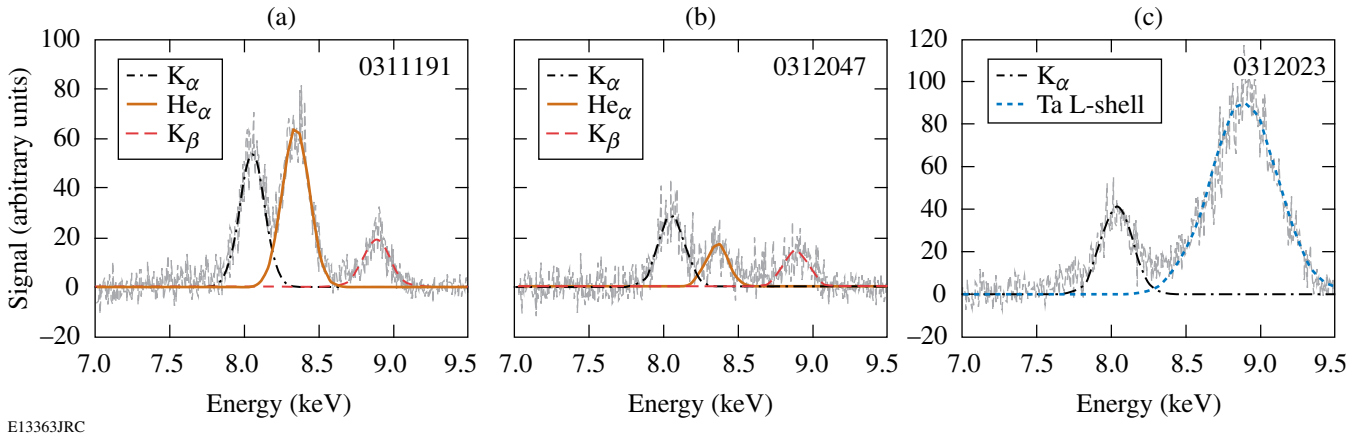

Figure 104.52
Copper K-shell spectra with the target's front side covered with a thin layer of different materials that leads to a suppression of the ionic line emission. (a) is without a cover layer, while (b) and (c) denote the results with a 1-μm-thick aluminum and with a 0.5-μm-thick tantalum layer, respectively. The He$_\alpha$ line emission is strongly reduced (b) and even absent (c) compared to the no cover layer (a), indicating that the hot plasma is generated in a thin layer on the target's front side. The laser energies, pulse duration, and intensity were 254 J (a), 227 J (b), 227 J (c), 0.7 ps, and ~1.5×10^{20} W/cm^2.

Analysis and Discussion

Two emission processes occur in these experiments: inner-shell emission and resonance-line emission. The K_α and K_β lines are emitted by inner-shell transitions when an L- or M-shell electron fills a vacancy in the K-shell, and the corresponding excess energy is radiated away by a photon in competition with Auger decay. X rays and energetic electrons may both produce inner-shell vacancies, assuming that the radiation has sufficient energy to excite above the K-edge (for Cu $h\nu > 9$ keV). Indirect inner-shell emission due to absorption of continuous x-ray radiation that is produced while suprathermal electrons decelerate in the target is, however, relatively negligible for elements with an atomic number <30.[39] Energetic electrons are the main contribution to K_α and K_β production in a high-intensity, ultrashort, laser–solid interactions with low- and mid-Z materials.[22,24] In contrast, the He_α and Ly_α lines are electronic transitions from the first excited to the ground level in the helium-like and hydrogen-like ions. Sufficient thermal plasma temperatures are required to generate these highly stripped ions. While the inner-shell radiation originates from the cold bulk material, the ionic lines are produced in hot plasmas, which is depicted in a schematic in Fig. 104.54. Resonance-line emission originates from a hot plasma on the laser target side while fast electrons generated by the laser–plasma interaction propagate into the cold bulk and produce the inner-shell emission.

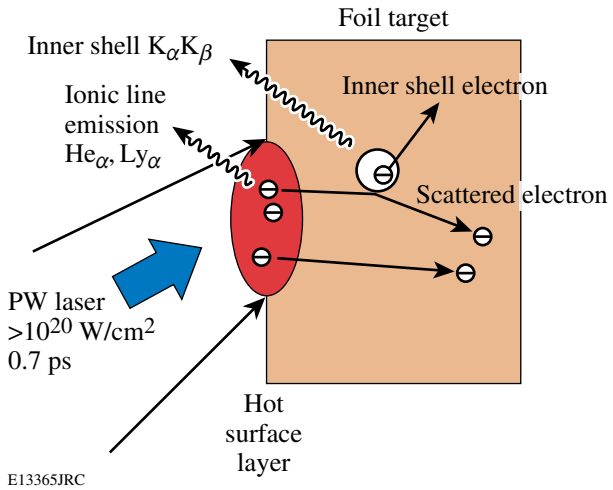

Figure 104.54
Schematic representation of the resonance and inner-shell emission generation process. The ionic lines stem from a hot surface layer while fast electrons produce the inner-shell emission.

1. Resonance-Line Emission From Hot Plasmas

Calculations with the commercially available *PrismSPECT* program[40] were performed to estimate the plasma conditions that lead to the ionic resonance-line emission from the hot plasma. *PrismSPECT* is a collisional-radiative code that takes all the necessary details of the excitation and de-excitation paths, opacity, and atomic physics into account. The plasmas are assumed to be in steady state, in nonlocal thermodynamic equilibrium conditions in slab geometry with a specified thickness, and have a homogeneous density and electron temperature. Time-dependent collisional-radiative calculations of the ionization dynamics of solid-density aluminum plasmas at $T_e = 1$ keV show that steady-state conditions are established within ~0.5 ps.[41] Similar time-dependant calculations performed for $T_e = 1$ keV and $n_e = 10^{23}$ cm^{-3} show the Cu plasma reaching steady state within ~1 ps.[42] Steady state is therefore a reasonable assumption for near-solid-density plasmas in our experiment. Suprathermal electrons were not included in the calculation. This assumption is supported by calculations of the charge-state distribution of a 1-keV, 10^{23} cm^{-3} Cu plasma including the ionization effect of a hot-electron component. The charge-state distribution is essentially given by the thermal plasma, and up to a fraction of 10% of hot electrons with an average energy of 3 MeV has no significant influence.[42] The overcoat measurements (Fig. 104.52) show that the hot plasma is formed from a layer that has initially $t \approx 1$-μm thickness at solid density. Figure 104.55(a) shows a comparison for the experimentally measured ionic K-shell emission for shot 0311271 (solid square symbols) to calculations for an electron density of $n_e = 2.3 \times 10^{24}$ cm^{-3}, $t = 1$ μm, and various electron temperatures between 1 keV and 3 keV. The electron density corresponds to a solid density of $n_{ion} = 8.5 \times 10^{22}$ cm^{-3} and an average degree of ionization of 27. The K_α and K_β lines are suppressed to allow a better comparison of the resonance-line emission to the calculations. The filter transmission of the 150-μm Cu foil was taken into account, and the calculated spectra were convolved with an instrumental resolution of 200 eV. The *PrismSPECT* calculation reveals that the measured He_α peak is a complicated array of lines including the He_α line, the intercombination line, dipole forbidden lines, and lithium-like ion satellite lines that merge together. The effective line width of this feature is ~90 eV at solid density and explains the slightly larger measured spectral width of ~220 eV for He_α. The ratio of the He_α and Ly_α lines is sensitive to the temperature and a good agreement is obtained for an electron temperature of 1.8 keV.

The ASE laser pulse pedestal causes some ablation of the front layer before the main laser pulse impinges on the target.

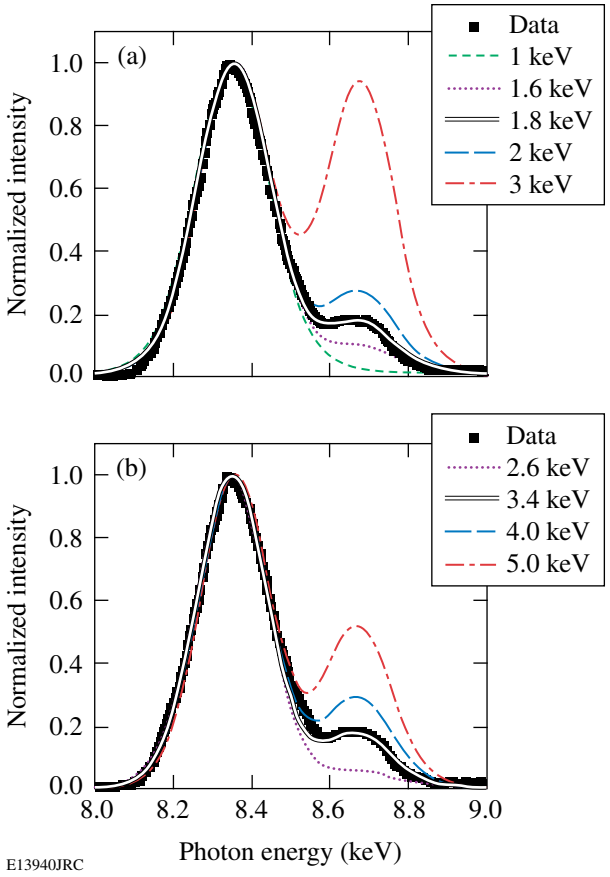

Figure 104.55
Comparison of the experimentally measured ionic K-shell emission (solid square symbols) to calculations with the computer program *PrismSPECT*[40] for (a) solid-density ($n_e \approx 2.3 \times 10^{24}$ cm^{-3}) 1-μm-thick plasma slab, and various electron temperatures between 1 keV and 3 keV. Figure (b) shows a comparison for an electron density of 2.3×10^{23} cm^{-3}, plasma slab thickness of 1 μm, and various electron temperatures between 2.6 keV and 5 keV.

The main pulse then interacts with less than solid density plasma and an increased density scale length. The density profile depends on the laser contrast, pulse profile, and hydrodynamic expansion of the preplasma. To model the density profile generated by the ASE pulse, a two-dimensional hydrodynamic simulation of the expansion and structure of the preplasma was performed using the Eulerian code POLLUX.[43] A 2.5×10^{13} W/cm^2 Gaussian temporal pulse shape was assumed with a 1.5-ns pulse duration. In the radial direction, a Gaussian-shaped intensity profile with a FWHM of 7 μm was used for the simulation. Figure 104.56 shows a lineout of the calculated electron-density profile along the target normal at the peak of the interaction pulse. The critical density expanded ~2 μm from the original surface. The interaction of the main pulse with relativistic intensities and the corresponding electron mass increase leads to a higher critical density than in the nonrelativistic case. A distance of ~1 μm is then calculated for the relativistic corrected critical density. The distance from the original target surface to the 10^{19} cm^{-3} contour is ~45 μm, which agrees well with the shadowgraph measurements. Preplasma formation on the Vulcan 100-TW laser has been previously experimentally and theoretically investigated.[37,44] Density scale lengths of ~3 μm and ~10 μm were determined at the critical density and at one-tenth of the critical density, respectively.

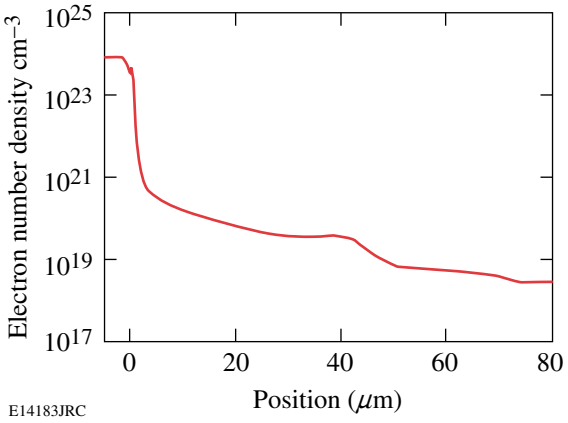

Figure 104.56
Calculated electron density profile along the target normal that is generated by an ASE prepulse; see text for details. The 2-D Eulerian code POLLUX[43] was used for the simulation.

The density profile shows that the ablated mass below critical density is a factor of ~10 smaller compared to the 1-μm layer from critical density up to solid density. Accordingly, the number of ionic line emitters in the ablation plume is negligible compared to the emitter number above critical density where most of the absorbed laser energy is deposited. Thermal energy transport into the target is estimated to be several microns deep with close to solid density based on the overcoating experiments. Figure 104.55(b) shows a comparison of measured and calculated spectra for $n_e = 2.3 \times 10^{23}$ cm^{-3}, $t = 1$ μm, and various temperatures with the best agreement at $T_e = 3.4$ keV. Not shown is the comparison for $n_e = 2.3 \times 10^{23}$ cm^{-3} and $t = 10$ μm, yielding $T_e = 2.6$ keV, which has roughly the same emitter number as the solid density, $t = 1$ μm calculation. Opacity effects in the blowoff plasma are negligible because of the low concentration of He- and H-like ions. The electron temperature is thus estimated to be in the range of 2 to 3 keV for a close-to-solid-density plasma and slab thickness between 1 and 10 μm. The number is in agreement with highly resolved Cu K-shell spectral measurements performed at similar experimental conditions yielding a front side electron temperature of ~2 keV.[45]

Two-dimensional opacity effects and heating of the underdense plasma by the short interaction pulse were not considered. Optical-field-ionized He- and H-like ion generation in the underdense plasma along the laser channel is negligible. Using a simple over-the-barrier suppression calculation for electric field ionization,[46] estimated saturation intensities of 2×10^{20} W/cm^2 and 7×10^{22} W/cm^2 are required to produce helium- and hydrogen-like copper ions with an ionization probability close to unity. The creation of He-like Cu ions by field ionization is therefore possible only at the highest accessible laser intensity. Ponderomotively accelerated electrons and ions in a radial direction[37] that might modify the charge-state distribution of the plasma as well as velocity gradients because of the tight-focusing condition and the resulting spherical expansion geometry that might affect the opacity[47] were not included in the analysis.

A precise comparison between the measured absolute He_α and Ly_α photon numbers and the predicted numbers by *PrismSPECT* are not straightforward and out of the scope of this article. A detailed knowledge of the angular emission characteristic, source area, and temporal emission characteristic is required. Laser plasmas are highly transient with strong spatial gradients in density and temperature, and a comparison to the measurement requires detailed multidimensional hydrodynamic simulations coupled to a multidimensional, time-dependent radiation transport model. An estimate of the source area may be obtained from measurements of Cu K_α images, typically yielding an area of 50 to 100 μm FWHM in diameter,[12,24] and from Ni Ly_α imaging measurements with ~30 μm spots that were obtained under similar experimental conditions.[48] Town *et al*., recently reported on simulations to calculate K_α images under similar experimental conditions and obtained agreement with measured K_α spot sizes.[49] Assuming an isotropic He_α and Ly_α emission and neglecting multidimensional and time-dependent opacity effects, the comparison of measured photon numbers and steady-state calculations for a solid-density, $t = 1$ μm surface layer plasma suggests average emission times of several picoseconds.

The increase in He_α emission with a laser intensity above 10^{18} W/cm^2 shown in Fig. 104.49 shows an energy transport growing with intensity into the solid-density plasma where electron–ion collisions create the ions in the hot-plasma environment. An enhanced energy transport into the solid results in higher temperatures and a larger fraction of He-and H-like Cu ions in the hot surface plasma. The absorption of the laser energy takes place in the density range close to the critical density and is dominated by collisionless absorption mechanisms that produce electrons with quasi-Maxwellian energy spectra and temperatures from hundreds of keV to several MeV for all intensities discussed here.[50] The angular distribution is generally into the target. The electron source parameters vary with the local intensity and therefore also have a spatial pattern related to the laser focal-spot intensity pattern. Energy transport by these electrons is highly complicated and, up to now, not fully understood. Their binary collision range is generally much greater than the thin layer, which is strongly heated. Several processes may contribute to localizing energy deposition in a surface layer. Simple ohmic potential due to the cold electron return current can limit electron penetration, as discussed by Bell *et al*.[19] Electrons can be trapped at the surface by their small Larmor radius in the surface region azimuthal thermoelectric B field generated by the axial increase of density and radial decrease of temperature (dB/dt scaling as $\nabla N \times \nabla T$), with the axial ambipolar electric field in the blowoff plasma causing a rapid radial drift (scaling as $E \times B$). This effect, well known from nanosecond experiments, particularly with CO_2 lasers, has been discussed in connection with petawatt-class, short-pulse experiments by Stephens *et al*.[12] and modeled recently by Mason *et al*.[51] Three-dimensional PIC simulations by Sentoku *et al*.,[16] have shown that there can be very strong collisionless energy deposition in a thin surface layer attributable to the "ohmic" heating effect of the return current due to anomalous resistivity induced by the scattering of the return current electrons on microscopic clumps of the B field generated by collisionless Weibel and two-stream instability. There is also evidence in PIC modeling by Adam *et al*.[52] and Ruhl[53] that the strongest filamentation occurs in a thin surface layer. These processes may all contribute to the observed thin, high-temperature layer, but further work is needed to establish their relative importance.

The energy required to create a significant amount of He-like and H-like Cu ions is estimated by assuming the mass of the hot layer to be equivalent to an ~1-μm-thick layer at solid density, as determined from the overcoat experiments. For example, an energy of ~3.5 J is needed to heat a mass of solid copper contained in a disk with a 50-μm diam and 1-μm thickness to ~3 keV and the resulting average charge state of 27. This is small compared to laser energies of the order of 100 J.

It should be noted that the spectral measurements indicate that K_α and He_α are two distinctive lines with no significant continuum merged between them. This is supported by highly resolved measurements with a crystal spectrograph under similar experimental conditions.[54] The upshift of K_α emission from partially ionized Cu ions has been discussed by Gregori

et al.[54] There is a small spectral shift as M-shell electrons are removed because of the heating of the bulk of the target by binary collisions of hot electrons and ohmic heating by the return current. It is indistinguishable in our low-resolution K_α spectra. Removal of L-shell electrons at higher temperatures gives larger shifts as the hot layer is heated and emission occurs at each stage of ionization. The He-like ion is, however, present over a wide temperature range and, in particular, during the emission occurring after the initial heating, leading to a dominant He_α spectral feature in our spectra. This heating partially ionizes the bulk, resulting in a K_α emission shifted to higher energies.

Measurements of the K-shell emission as a function of foil thickness between 30 μm and 1 μm for a constant laser intensity of ~3×10^{18} W/cm^2 show that the K_α emission remains about constant with diminishing foil thicknesses down to 3 μm. This is expected if no other hot-electron energy-loss mechanisms become significant; the electron temperature of the foil is so low that ionization does not significantly affect the L-shell, and the majority of the electrons are refluxing from an electrostatic sheath field. The decreasing yield for targets thinner than 3 μm might imply that a significant amount of cold material is depleted. Another possible explanation is that, for very small volume targets, additional energy dissipation channels draining hot-electron energy might become important and influence the K_α signal. A possible channel is energy transfer into accelerated ions, which is enhanced in very thin targets.[36] The K_β yield is expected to be more sensitive to a temperature increase of the bulk of the target since K_β is eliminated when the M-shell is ionized, which might explain the decrease by factor of ~4 from 30 μm to 20 μm while no change is measured for K_α. The target volume changed by a factor of ~40 because a 500×500 μm^2 foil area was used at 30-μm thickness while 100×100 μm^2 was applied for the thinner targets. R. Snavely *et al.*, recently reported on similar observations and extensively discussed how the laser heating of very small target volumes affects the inner-shell emission.[55] The resonance-line emission from the 1-μm top layer is not expected to be significantly affected by the foil thickness. Nevertheless, varying He_α emission is observed with a peak at 5-μm thickness. This variability may be due to slight changes in the laser conditions from shot to shot. As shown in the measurement in Fig. 104.49, the He_α signal is more sensitive to the applied laser intensity than is the inner-shell emission.

2. Inner-Shell Emission

Implicit-hybrid PIC simulations with the code *LSP*[56] were performed to study inner-shell production with various foil areas in the range from 500×500 μm^2 to 100×100 μm^2 and thicknesses of 20 μm to 5 μm, similar to the simulations recently reported by R. Town.[49] No significant change of K_α yield with the target area and thickness is calculated, which is attributed to the refluxing of most of the hot electrons at the target boundaries.[36] These calculations have solved the Maxwell equations coupled with the equations of motion for multiple particle species in a two-dimensional cylindrical geometry. The initially cold ions and bulk electrons of the target were modeled with fluid equations, and the hot laser-produced electrons were treated kinetically. The propagation and interaction of the high-intensity laser was not included, rather, the hot electrons were introduced into the calculation in an *ad hoc* manner by converting or "promoting" bulk electrons within a skin depth on the front of the target into the kinetic species. The kinetic electrons were given an isotropic Gaussian distribution in momentum space with a temperature that was determined by the ponderomotive potential of the local laser intensity.[13] The local conversion rate was determined by assuming a 10% coupling efficiency from the local incident laser power into hot electrons. The laser spot shape was taken to be the same as in the experiment, both spatially and temporally. Although the heating of the target was modeled, the ionization of the target material was ignored.

The measured K_α photon numbers, per unit laser energy, are in general agreement with other experiments.[20,24] In Ref. 20, 2×10^{11}/J K_α photons were reported for 8-μm-thick Cu foil targets irradiated with 528-nm laser pulses at intensities of ~10^{19} W/cm^2. Similar numbers were reported in Ref. 24; however, these experiments used thick targets where the reabsorption of the K_α photons was strong, and the controlling mechanism was the interplay between electron-penetration depth relative to the K_α photon-attenuation length. With the targets considered here, reabsorption gives a modest correction; e.g., for solid copper, the transmission fraction f_{trans} is estimated to be 0.91, 0.69, and 0.58 for foil thicknesses of d = 5, 20, and 30 μm respectively.

The expected number of photons generated N_k can be computed by integrating along the path of electrons whose initial energies are described by an energy distribution $f(E_0)$ so long

as the electron stays within the material, its energy loss is accurately described with a continuous slowing down formula (dE/ds), and that cold cross sections σ_k for K-shell ionization are appropriate (note that for copper, only direct K-shell ionization is significant[39]). The yield N_k is then given by

$$N_k = N_e \int_0^\infty dE_0 f(E_0) \int_{E_0}^0 dE \omega_k n_{Cu} \sigma_k \left(\frac{dE}{ds}\right)^{-1}, \quad (1) \text{ and } (2)$$

$$= N_e \int_0^\infty dE_0 f(E_0) \int_0^{s(E_0)} ds \omega_k n_{Cu} \sigma_k,$$

where N_e is the total number of hot electrons, $\omega_k = 0.425$ is the fluorescence yield, and n_{Cu} is the number density of copper atoms in the target. From this model the electron-to-K_α photon-generation efficiency $\eta_{e\to k}$ is determined. This efficiency is defined according to $E_k = \eta_{e\to k} E_e$, where the energy in the electrons is given by $E_e = N_e \int Ef(E)dE$ and in K_α photons by $E_k = \varepsilon_k N_k$ with ε_k being the fluorescence energy (8.05 keV for copper K_α). This simple model accounts only for the collisional energy loss and neglects ohmic effects and energy transfer to fast ions.

A direct comparison between the experimental production efficiency (yield/laser energy) and the calculated generation efficiency is not straightforward. The experimentally observable quantity is $N_{k,\mathrm{obs}}$ from which the efficiency may be computed as

$$\eta_{e\to k} = \frac{\varepsilon_k \left(N_{k,\mathrm{obs}} / f_{\mathrm{trans}}\right)}{E_L} \frac{1}{\eta_{L\to e}} \quad (3)$$

only if the transmission fraction and the hot-electron production efficiency $\eta_{L\to e} = E_e/E_L$ are known. Here, E_L is the energy in the laser pulse. The transmission fraction can be easily computed, but the electron-production efficiency is uncertain. Assuming that the hot-electron density within the foil is uniform, the K_α photon transmission fraction is estimated by $f_{\mathrm{trans}} = \left(L_a/d\right)\left[1 - \exp\left(-d/L_a\right)\right]$ with the attenuation length L_a = 25 μm. The predicted efficiency, obtained using Eq. (1), further requires specification of the hot-electron spectrum $f(E)$.

The predicted total K_α energy of the model divided by the laser energy, together with experimental data, are shown in Fig. 104.57 for different $\eta_{L\to e}$ assuming exponentially distributed electron energies, $f(E)dE = \left(1/T\right)/\exp\left(-E/T\right)dE$, and using slowing down and cross section data from the ITS code.[57] The total K-shell ionization cross section is from Ref. 58 and, unlike the cross section in Ref. 39, it is valid for relativistic electron energies. For highly relativistic electrons, the cross section increases with particle energy. In Ref. 59, an increased K_α yield was measured with laser intensities above 10^{19} W/cm^2 and attributed to an enhanced K-shell ionization cross section for relativistic electrons. In contrast to this work, an increase in the K_α yield with the laser intensity is not observed. Calculations have also been performed with a 3-D relativistic distribution function, leading to slightly higher predicted efficiencies, but with no change to our overall conclusions. Although different intensity temperature scaling appears in the literature,[29,60] in Fig. 104.57 we have chosen the ponderomotive scaling of Wilks,[13,61]

$$T_{\mathrm{MeV}} = 0.511\left[\left(1 + I_{18}\lambda_{\mu\mathrm{m}}^2 / 1.37\right)^{1/2} - 1\right],$$

to connect the laser intensity to the hot-electron temperature. No spatial-laser intensity distribution was taken into account in this calculation.

In Fig. 104.57, the experimental data is almost independent of laser intensity, except at the highest laser intensity, $I = \sim 3 \times 10^{20}$ W/cm^2. This independence of efficiency on hot-electron temperature, over the experimental range of intensities, is a consequence of Eq. (1), displayed by the solid model curves. The efficiency is determined by the relative importance of energy loss due to nonionizing collisions and the cross section for K-shell ionization. The latter is quite flat for energies above 100 keV,[62] while the collisional cross section drops with increasing energy. The electron range is not restricted by the target thickness for the solid curve in order to mimic the effect of electron refluxing. The net result is that the number of photons produced per unit electron energy is only a weakly increasing function. The solid curves can be made to agree quantitatively with the experimental data if we select an ~8% hot-electron coupling efficiency. This is lower than the $\eta_{L\to e}$ ~ (20% to 40%) usually quoted in the literature for these intensities, e.g., in Ref. 4 (upper solid curve). Given the relative large uncertainty in the experimental points because of the CCD calibration uncertainty, the current measurement is in rough agreement with the previous measurements. In addition, the calculated 8% hot-electron coupling efficiency should be regarded as a lower bound because fast-electron energy loss into other channels, such as energy transfer into fast ions and ohmic effects, were not included in the model. Accounting for additional losses would shift the theoretical curves downward, leading to a higher $\eta_{L\to e}$ for the measurement.

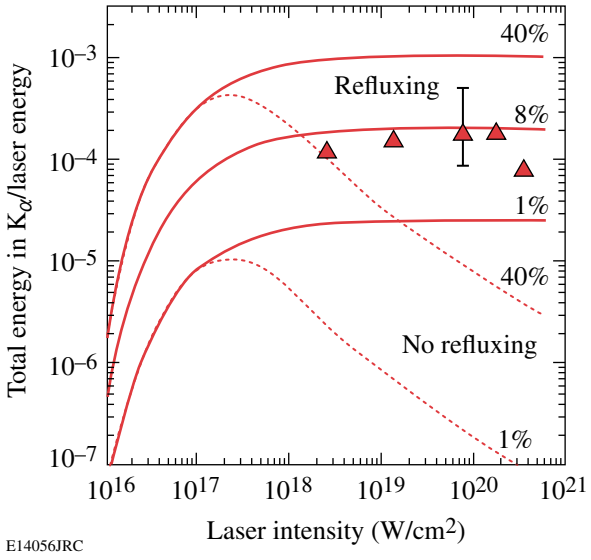

Figure 104.57
Total energy in K_α photons normalized to laser energy in the central laser spot as a function of laser intensity. The solid triangles are the experimental data points. The solid curves correspond to the model described in **Inner-Shell Emission** (p. 216) with perfect confinement of the hot electrons (refluxing) and with a hot-electron conversion efficiency of 40%, 8%, and 1%. The dotted curves correspond to the case (40% and 1%) with no refluxing, as described in the text. An 8% hot-electron coupling efficiency is calculated, which should be regarded as a lower bound because fast-electron energy loss into other channels, such as energy transfer into fast ions and ohmic effects, were not included in the model. A representative error bar shows the measured efficiency uncertainty.

The dotted curves illustrate the effect of truncating the electron path length s in the integral, Eq. (2), whenever it exceeds the target thickness $s(E_0) \rightarrow \min[s(E_0), d]$. Electrons in Cu have ranges from ~1 μm to ~700 μm for energies from 10 keV to 1 MeV.[57] Only a small fraction of the fastest electrons can escape out the foil, resulting in quickly charging up the target and confining the rest of the electrons that are reflected back from surface sheath fields. Refluxing has previously been discussed in the context of proton generation, showing the importance of the recirculation of the MeV electrons on the electrostatic fields that accelerate protons to multi-MeV energies.[36] As expected, ignoring refluxing in the model shows disagreement with the experimental data by an order of magnitude or more. Physically, the solid curves correspond to the case where hot electrons are confined within the target due to reflection or "refluxing" from surface sheath fields until it is stopped, whereas the dashed curves correspond to the case where the electron and its energy are lost as soon as its path length equals the target thickness. Refluxing has been observed in PIC calculations, leading to a yield that is independent of target volume.

The fact that the experimental efficiencies are lower than might be expected based on the simple refluxing model presented here might have several causes: refluxing might not be perfect. With a significant loss fraction, the range of the electrons might be overestimated (which leads to higher efficiencies) due to "anomalous" stopping mechanisms related to large, self-generated magnetic and electric field fluctuations, presumably becoming more important at higher intensities.[16] Target heating might invalidate the use of the cold cross sections.

Summary and Conclusions

For the first time, He_α and Ly_α lines in the K-shell emission of solid Cu targets irradiated with a 0.7-ps petawatt laser beam were observed at intensities >10^{20} W/cm^2. This is attributed to the formation of a ~2 to 3 keV near-solid-density hot plasma on the laser irradiation target side. A suppression of the ionic line emission is observed when the Cu targets are coated with either a 1-μm thin layer of aluminum or with a 0.5-μm tantalum layer, indicating that the strongest heating is confined to a thin layer.

Measurements of the K-shell emission as a function of foil thickness between 30 μm and 1 μm for a constant laser intensity of ~3×10^{18} W/cm^2 and ~10-ps pulses show that the He_α emission varies by a factor of ~4 with a peak at 5-μm thickness, while the K_α yield stays about constant. A decreased K_α yield measured for targets thinner than 3 μm might be explained by a stronger heating of the small target volume and an increased hot-electron energy transfer into ions. Changing laser conditions especially affecting the surface layer could cause the variation of the He_α emission. The current data set is limited by its small sample size, and more shots are necessary to investigate this observation.

The K-shell emission of solid Cu foil targets was studied as a function of laser intensity between 2×10^{18} W/cm^2 up to 3×10^{20} W/cm^2 in low-area (~0.5×0.5 to 2×2 mm^2) thin foils (~20 to 30 μm) and 0.7-ps pulses. The yield of the ionic lines strongly increases with laser intensity such that, at the maximum intensity, the spectrum is dominated by the He_α emission. An approximately constant yield of ~1×10^{11} photons/J and ~1×10^{10} photons/J were measured for the K_α and K_β inner-shell emission, respectively, between intensities of 2×10^{18} W/cm^2 and 1×10^{20} W/cm^2. Above 1×10^{20} W/cm^2, the inner-shell emission yield drops. A comparison of the measured intensity scaling of the K_α yield with a model shows that refluxing of suprathermal electrons and their confinement in the target volume is crucial to explain these results. Calculations that ignore refluxing show a strongly decreasing K_α yield with

laser intensity and disagree with the experimental data by more than an order of magnitude.

ACKNOWLEDGMENT

This work was supported by the U.S. Department of Energy Office of Inertial Confinement Fusion under Cooperative Agreement No. DE-FC52-92SF19460, the University of Rochester, the New York State Energy Research and Development Authority, and the University of California Lawrence Livermore National Laboratory under contract No. W-7405-Eng-48 UCRL_PRES213395. The support of DOE does not constitute an endorsement by DOE of the views expressed in this article.

REFERENCES

1. M. Tabak *et al*., Phys. Plasmas **1**, 1626 (1994).
2. O. L. Landen *et al*., Rev. Sci. Instrum. **72**, 627 (2001).
3. H.-S. Park *et al*., Rev. Sci. Instrum. **75**, 4048 (2004).
4. K. B. Wharton *et al*., Phys. Rev. Lett. **81**, 822 (1998).
5. S. P. Hatchett *et al*., Phys. Plasmas **7**, 2076 (2000).
6. K. Yasuike *et al*., Rev. Sci. Instrum. **72**, 1236 (2001).
7. R. Kodama *et al*., Phys. Plasmas **8**, 2268 (2001).
8. M. H. Key, M. D. Cable, T. E. Cowan, K. G. Estabrook, B. A. Hammel, S. P. Hatchett, E. A. Henry, D. E. Hinkel, J. D. Kilkenny, J. A. Koch, W. L. Kruer, A. B. Langdon, B. F. Lasinski, R. W. Lee, B. J. MacGowan, A. MacKinnon, J. D. Moody, M. J. Moran, A. A. Offenberger, D. M. Pennington, M. D. Perry, T. J. Phillips, T. C. Sangster, M. S. Singh, M. A. Stoyer, M. Tabak, G. L. Tietbohl, M. Tsukamoto, K. Wharton, and S. C. Wilks, Phys. Plasmas **5**, 1966 (1998).
9. P. A. Norreys *et al*., Phys. Plasmas **6**, 2150 (1999).
10. K. A. Tanaka *et al*., Phys. Plasmas **7**, 2014 (2000).
11. J. A. Koch *et al*., Phys. Rev. E **65**, 016410 (2001).
12. R. B. Stephens *et al*., Phys. Rev. E **69**, 066414 (2004).
13. S. C. Wilks *et al*., Phys. Rev. Lett. **69**, 1383 (1992).
14. B. F. Lasinski *et al*., Phys. Plasmas **6**, 2041 (1999).
15. L. Gremillet, G. Bonnaud, and F. Amiranoff, Phys. Plasmas **9**, 941 (2002).
16. Y. Sentoku *et al*., Phys. Rev. Lett. **90**, 155001 (2003).
17. A. R. Bell and R. J. Kingham, Phys. Rev. Lett. **91**, 035003 (2003).
18. A. J. Kemp *et al*., Phys. Plasmas **11**, L69 (2004).
19. A. R. Bell *et al*., Plasma Phys. Control. Fusion **39**, 653 (1997).
20. T. Feurer *et al*., Phys. Rev. E **56**, 4608 (1997).
21. R. Kodama *et al*., Nature **432**, 1005 (2004).
22. H. Chen, B. Soom, B. Yaakobi, S. Uchida, and D. D. Meyerhofer, Phys. Rev. Lett. **70**, 3431 (1993).
23. A. Rousse *et al*., Phys. Rev. E **50**, 2200 (1994).
24. D. C. Eder *et al*., Appl. Phys. B **70**, 211 (2000).
25. H. R. Griem, *Spectral Line Broadening by Plasmas* (Academic Press, New York, 1974).
26. J. L. Collier *et al*., *Central Laser Facility Annual Report 2002/2003*, 168, Rutherford Appleton Laboratory, Chilton, Didcot, Oxon, England, RAL Report No. RAP-TR-2003-018 (2003).
27. C. N. Danson *et al*., J. Mod. Opt. **45**, 1653 (1998).
28. P. K. Patel, M. H. Key, A. J. Mackinnon, H.-S. Park, R. Shepherd, H. Chen, R. A. Snavely, N. Izumi, J. Kuba, J. Koch, S. C. Wilks, M. May, R. Van Maren, J. A. King, B. Zhang, K. Akli, R. Freeman, S. Kar, L. Romagnani, M. Borghesi, C. Stoeckl, W. Theobald, R. Eagleton, M. Mead, R. J. Clarke, R. Heathcote, P. A. Brummitt, D. R. Neville, D. Neely, and R. Stephens, *Central Laser Facility Annual Report 2003/2004*, 34, Rutherford Appleton Laboratory, Chilton, Didcot, Oxon, England, RAL Report No. RAL-TR-2004-025 (2004).
29. F. N. Beg *et al*., Phys. Plasmas **4**, 447 (1997).
30. C. Stoeckl, W. Theobald, T. C. Sangster, M. H. Key, P. Patel, B. B. Zhang, R. Clarke, S. Karsch, and P. Norreys, Rev. Sci. Instrum. **75**, 3705 (2004).
31. M. Nishiuchi *et al*., in *EUV, X-Ray, and Gamma-Ray Instrumentation for Astronomy IX*, edited by O. H. Siegmund and M. A. Gummin (SPIE, Bellingham, WA, 1998), Vol. 3445, pp. 268–277.
32. D. H. Lumb and A. D. Holland, Nucl. Instrum. Methods Phys. Res. A **273**, 696 (1988).
33. H.-S. Park, Lawrence Livermore National Laboratory, private communication (2005).
34. J. A. Bearden, Rev. Mod. Phys. **39**, 78 (1967).
35. R. L. Kelly, J. Phys. Chem. Ref. Data **16**, 651 (1987).
36. A. J. Mackinnion *et al*., Phys. Rev. Lett. **88**, 215006 (2002).
37. H. Habara *et al*., Phys. Rev. E **70**, 046414 (2004).
38. D. E. Post *et al*., At. Data Nucl. Data Tables **20**, 397 (1977).
39. M. Green, Solid-State Electron. **3**, 314 (1961); M. Green and V. E. Cosslett, J. Phys. D **1**, 425 (1968).
40. Prism Computational Sciences, Inc., Madison, WI, 53711.
41. J. J. MacFarlane *et al*., in *Inertial Fusion Sciences and Applications 2003*, edited by B. A. Hammel *et al*. (American Nuclear Society, La Grange Park, IL, 2004), pp. 457–460.
42. H. K. Chung, Lawrence Livermore National Laboratory, private communication (2005).
43. G. J. Pert, J. Comput. Phys. **43**, 111 (1981).

44. M. I. K. Santala *et al*., Phys. Rev. Lett. **84**, 1459 (2000).

45. M. Key *et al*., presented at the 8th International Workshop on Fast Ignition of Fusion Targets, Tarragona, Spain, 29 June–1 July 2005.

46. S. Augst, D. Strickland, D. D. Meyerhofer, S. L. Chin, and J. H. Eberly, Phys. Rev. Lett. **63**, 2212 (1989).

47. L. Labate *et al*., Phys. Plasmas **12**, 083101 (2005).

48. M. Key, Lawrence Livermore National Laboratory, private communication (2005).

49. R. P. J. Town, presented at the International Workshop on Fast Ignition and High Field Physics, Kyoto, Japan, 25–29 April 2004 (Paper P2633); R. P. J. Town, presented at the 8th International Workshop on Fast Ignition of Fusion Targets, Tarragona, Spain, 29 June–1 July 2005.

50. P. Gibbon and E. Förster, Plasma Phys. Control. Fusion **38**, 769 (1996).

51. R. J. Mason, E. S. Dodd, and B. J. Albright, Phys. Rev. E **72**, 015401(R) (2005).

52. J.-C. Adam, A. Héron, and G. Laval, presented at the International Workshop on Fast Ignition and High Field Physics (FIHFP 2004), Kyoto, Japan, 25–29 April 2004 (Paper P2630).

53. H. Ruhl *et al*., presented at the International Workshop on Fast Ignition and High Field Physics (FIHFP 2004), Kyoto, Japan, 25–29 April 2004 (Paper P2631).

54. G. Gregori *et al*., Contrib. Plasma Phys. **45**, 284 (2005).

55. R. Snavely *et al*., presented at the 8th International Workshop on Fast Ignition of Fusion Targets, Tarragona, Spain, 29 June–1 July 2005.

56. D. R. Welch *et al*., Nucl. Instrum. Methods Phys. Res. A **464**, 134 (2001).

57. M. J. Berger, in *Methods in Computational Physics: Advances in Research and Applications*, edited by B. Alder, S. Fernbach, and M. Rotenberg, Volume 1: Statistical Physics (Academic Press, New York, 1963), pp. 135–215.

58. H. Kolbenstvedt, J. Appl. Phys. **38**, 4785 (1967).

59. F. Ewald, H. Schwoerer, and R. Sauerbrey, Europhys. Lett. **60**, 710 (2002).

60. D. W. Forslund, J. M. Kindel, and K. Lee, Phys. Rev. Lett. **39**, 284 (1977).

61. G. Malka and J. L. Miquel, Phys. Rev. Lett. **77**, 75 (1996).

62. C. Hombourger, J. Phys. B **31**, 3693 (1998).